Bubbles trapped in a fluidized bed: Trajectories and contact area

Raphaël Poryles,[1] Valérie Vidal,[1] and Germán Varas[2,*]

[1]*Laboratoire de Physique, École Normale Supérieure de Lyon, Université de Lyon–CNRS, 46 Allée d'Italie, 69364 Lyon Cedex 7, France*

[2]*Instituto de Fisica, Pontificia Universidad Católica de Valparaiso, Avenida Universidad 330, Valparaiso, Chile*

(Received 21 December 2015; published 22 March 2016)

This work investigates the dynamics of bubbles in a confined, immersed granular layer submitted to an ascending gas flow. In the stationary regime, a central fluidized zone of parabolic shape is observed, and the bubbles follow different dynamics: either the bubbles are initially formed outside the fluidized zone and do not exhibit any significant motion over the experimental time or they are located inside the fluidized bed, where they are entrained downwards and are, finally, captured by the central air channel. The dependence of the air volume trapped inside the fluidized zone, the bubble size, and the three-phase contact area on the gas injection flow rate and grain diameter are quantified. We find that the volume fraction of air trapped inside the fluidized region is roughly constant and of the order of 2%–3% when the gas flow rate and the grain size are varied. Contrary to intuition, the gas-liquid-solid contact area, normalized by the air injected into the system, decreases when the flow rate is increased, which may have significant importance in industrial applications.

DOI: 10.1103/PhysRevE.93.032904

I. INTRODUCTION

Ground fluidization is a process widely encountered in nature. It can be triggered either by an external perturbation—such as a seismic wave in the case of soil failure due to a strong earthquake [1]—or by the penetration of a fluid (liquid or gas) into unconsolidated ground. The latter phenomenon, which is referred to as "venting," displays many examples in nature, from pockmarks [2,3] and mud volcanoes [4–6] to kimberlite pipes [7–9]. These processes often involve a three-phase flow, with a granular solid phase, saturated or not, and the infiltration of either a gas or another liquid phase. The strong mixing between the phases is a direct consequence of fluidization and has inspired many ecological or industrial applications by mankind. Among these, two societal challenges are air sparging for aquifer sediment decontamination and ground remediation [10–12] and multiphase catalytic reactors, including stirred tanks and slurry bubble columns [13,14]. In both processes, increasing the contact area among the three phases is the main issue in optimizing the reactions.

Due to the complexity of soil structure [15], many models have been developed in the laboratory to investigate the invasion dynamics of a fluid inside a dry [16–18] or immersed [19–27] granular medium and the conditions for its subsequent fluidization. The experiments are performed either at an imposed constant flow rate or overpressure for the injected fluid. The invasion dynamics depends strongly on these parameters, as well as on the initial packing fraction of the bed. It has been shown that for a low injection rate, the fluid crosses the granular matrix without moving the grains significantly, as in a rigid porous medium, while at a high injection rate, the forces exerted by the fluid on the grains are strong enough to trigger instabilities and, possibly, lead to fluidization [21–23,26]. In such fundamental studies, buoyancy-driven systems are not always considered (see, for instance, [24] and [25]), although gravity has a crucial influence on hazard mitigation [10–12] or industrial processes [13,14].

Previous studies have investigated the shape and dynamics of the fluidized zone generated by a single gas injection at the bottom of an immersed granular layer. It has been shown that this fluidized region reaches a stationary shape of parabolic contour [10,11,27–33]. It is formed by a global grain motion which, in a two-dimensional (2D) vertical cell, takes the form of two convective rolls on both sides of the central gas rise [27,32]. The similarity of this parabolic region with the invasion zone in a fixed, porous medium is discussed in Ref. [27]. Contrary to the intuition, small bubbles trapped in this region follow the downward grain motion [27,31,32]. However, their dynamics has scarcely been investigated, although previous attempts have been made in dense, nonfluidized beds [34–36].

In this work, we focus on the dynamics and global characteristics of bubbles trapped in the fluidized zone generated by a single air injection point at the bottom of a water-saturated granular layer. In particular, we investigate under what conditions a bubble remains permanently trapped in the system or is captured by the central air rise. We define global parameters such as the air volume fraction in the fluidized region and the three-phase contact area in the stationary state and quantify their variations as a function of the flow rate and grain size.

II. EXPERIMENTAL SETUP

The experimental setup (Fig. 1) consists of a vertical Hele-Shaw cell (glass plates 40 × 30 cm, gap $e = 2$ mm) filled with particles immersed in water. The particles are polydisperse, spherical glass beads (Sovitech glass spheres), sieved to obtain four batches with particle diameters $d = 200$–250, 250–425, 600–710, and 710–965 μm. The grain size distribution is measured by means of a microscope (Optika B-163) and roughly displays a Gaussian shape [27]. The mean value and standard deviation of the particles diameter are therefore determined for each batch (Table I). In the following, we use these values to refer to the grain diameters $d = 218 \pm 17$, 318 ± 44, 631 ± 37, and 802 ± 68 μm, respectively.

*german.varas@pucv.cl

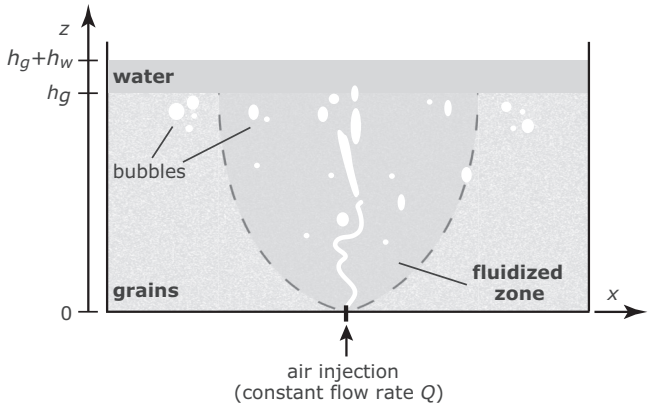

FIG. 1. Sketch of the experimental setup. A vertical Hele-Shaw cell is filled with grains immersed in water. Air is injected at the bottom at a constant flow rate Q. In the stationary regime, the central air rise forms a fluidized zone (see text). Bubbles are either trapped outside or entrained by the granular convection inside the central fluidized region.

To ensure reproducible experiments, the initial condition is set as follows. A fixed amount of grains is poured in the cell, which is then entirely filled with water, closed, and flipped over. When the sedimentation is almost complete, the cell is flipped back to its original vertical position. After sedimentation, the grain's free surface is gently smoothed with a thin pole, to obtain a horizontal free surface at a given height h_g (Fig. 1). This method allows us to remove all the bubbles from the initial immersed granular layer, and ensures a reproducible initial random loose packing fraction of the grains. Water is then removed from the system with a syringe, until only a shallow water layer (height h_w) remains above the granular bed (Fig. 1). Note that a small h_w makes it possible to avoid particle advection in the above liquid layer and the subsequent formation of a crater at the surface [37]. In all our experiments, the granular bed and water layer heights are fixed to $h_g = 20$ cm and $h_w = 2$ cm, respectively.

At $t = 0$ s, air is injected at a constant flow rate Q from a nozzle (inner diameter, 1 mm) located at the bottom center of the cell. The flow rate Q is fixed in the range 0.16–3.3 mL/s by a digital mass flow controller (M+W Instruments model D-6311). An LED panel ensures a constant backlight. Images of the experimental cell are recorded with a camera (PixeLINK model PL-B741U; 1280×800 px^2) at a frame rate of one image every 10 s, allowing us to follow the system evolution over long times (typically, 20 h).

TABLE I. Grain diameters from sieving and from measurements (average and standard deviation from a Gaussian fit of the grain size distribution; see [27]).

d (from sieving)	d (measured)
200–250 μm	218 ± 17 μm
250–425 μm	318 ± 44 μm
600–710 μm	631 ± 37 μm
710–965 μm	802 ± 68 μm

III. BUBBLE DYNAMICS

Previous works have pointed out that, independently of the initial air invasion regime at short times (percolation or fracture), similar three-phase systems develop a fluidized zone of parabolic shape, characterized by a central air channel and two lateral granular convection rolls [27,31–33]. In this section, we focus on the dynamics of the bubbles located either inside or outside the fluidized zone.

A. Spatiotemporal diagrams

Due to the backlight and the confinement in the vertical Hele-Shaw cell, bubbles crossing the granular layer appear white or light gray in the images, in contrast to grains which appear dark gray [see, for instance, Figs. 2(b) and 2(d)]. To follow the bubble dynamics, we introduce two variables computed from the binarized image sequence,

$$\xi_x(x,t) = \sum_z \mathrm{I}(x,z,t), \tag{1}$$

$$\xi_z(z,t) = \sum_x \mathrm{I}(x,z,t), \tag{2}$$

where $\mathrm{I}(x,z,t)$ is the intensity at coordinates (x,z) and time t, and the sum is performed over the whole experimental time (typically, 20 h). Due to the binarization, $\mathrm{I}(x,z,t) = 1$ for a bubble; otherwise, $\mathrm{I}(x,z,t) = 0$. The normalized variables are then written $\bar{\xi}_x = \xi_x(x,t)/\max(\xi_x(x,t))$ and $\bar{\xi}_z = \xi_z(z,t)/\max(\xi_x(x,t))$, where $\max(\xi_x(x,t))$ and $\max(\xi_x(x,t))$ are computed over the total experimental time. $\bar{\xi}_x(x,t)$ and $\bar{\xi}_z(z,t)$ therefore represent the probability that a bubble is located on a vertical, $x = $ const. (horizontal, $z = $ const.) line at time t.

Figures 2(a) and 2(c) display the spatiotemporal diagrams of $\bar{\xi}_x$ (upper panels) and $\bar{\xi}_z$ (lower panels) for two flow rates. The central air channel is clearly distinguishable in the spatiotemporal diagram of $\bar{\xi}_x$, which exhibits a strong signal around $x = 0$, at the vertical of the air injection point. The fluctuations of this central signal, corresponding to fluctuations of the central air channel geometry, are the consequence of sporadic events during which the gas in the channel explores the fluidized zone laterally. These lateral bursts can create additional bubbles, which are further entrained by the granular convection motion and eventually captured back by the central air channel [see, for example, the signature of bubble formation at $t \simeq 13$ h; Fig. 2(a), upper panel]. The white region up to $z \simeq 1$ cm [Figs. 2(a) and 2(c), lower panels] is the signature of an air finger, starting from the injection nozzle, above which we observe bubble fragmentation and lateral exploration—leading to gray, noisy background in the spatiotemporal diagram representing $\bar{\xi}_z(z,t)$.

Interestingly, the majority of the bubbles trapped inside the fluidized zone on both sides of the central air channel [dark-gray lines in Figs. 2(a) and 2(c)] are formed at the beginning of the experiment. Indeed, the initial gas invasion pattern (either percolation or fracture) explores a wide region of the granular bed, and many bubbles get trapped in this process, before the formation of the fluidized zone and the stabilization of the central air channel. These bubbles can be classified into two categories: (i) if the bubbles are initially

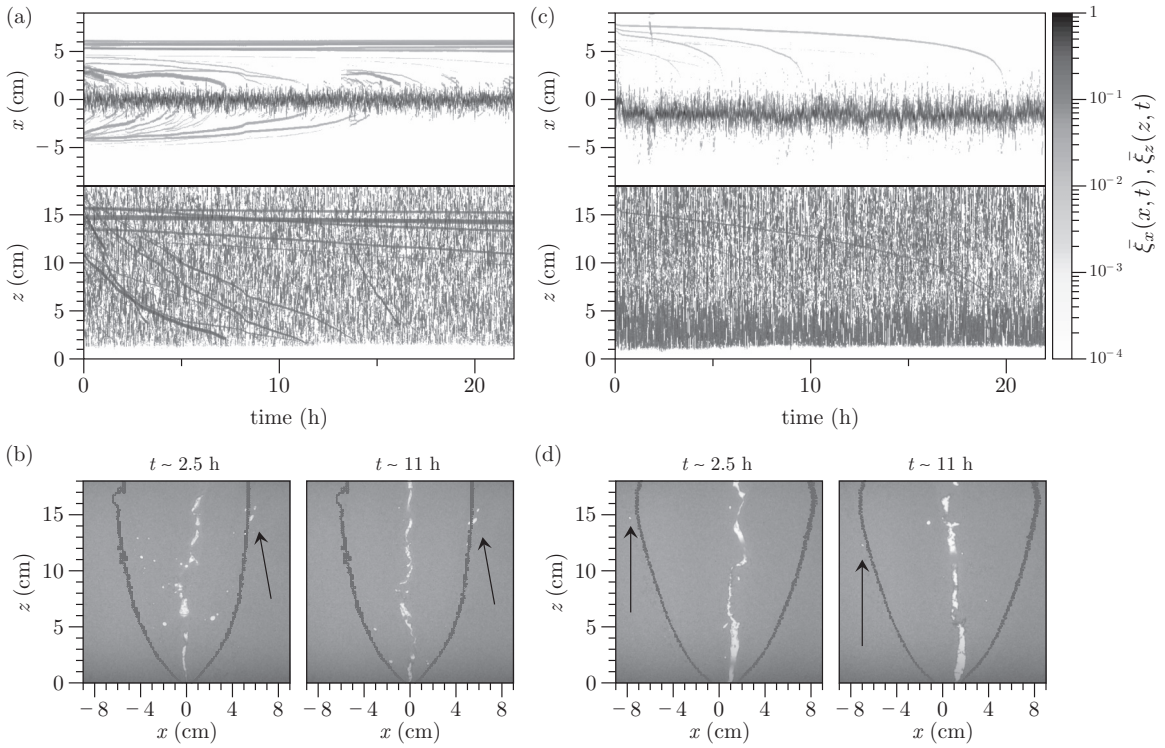

FIG. 2. Spatiotemporal diagrams and images of the experiment at different times ($t = 2.5$ h and $t = 11$ h) for different injection flow rates: (a, b), $Q = 0.66$ mL/s; (c, d) $Q = 1.98$ mL/s. The central air channel and bubble trajectories can be clearly seen in the spatiotemporal diagram (a, c). The dark-gray line on the images (b, d) indicates the contour of the fluidized zone (see text); the black arrows (b, d) point out bubbles trapped outside the fluidized zone, which are trapped permanently or exhibit a very slow motion when close to the fluidized-zone boundary [$d = 318 \pm 44$ μm].

formed inside the fluidized zone, they are entrained by the granular convection and, after some time, captured by the central air channel [curved dark-gray lines; Figs. 2(a) and 2(c), upper panels]; and (ii) if the bubbles are initially formed outside the fluidized zone, they remain trapped in the system and do not exhibit any significant motion [horizontal dark-gray lines; Fig. 2(a), upper panel].

Figures 2(b) and 2(d) show two pictures of the experiment corresponding to Figs. 2(a) and 2(c), respectively, taken at $t = 2.5$ h and $t = 11$ h. Gray lines in the pictures indicate the boundary of the fluidized zone (see Sec. IV). If the bubbles are located inside the fluidized zone [gray line in Figs. 2(b) and 2(d)], they are eventually captured by the central air channel. Examples of bubbles initially trapped outside, but close to the fluidized zone, in the apparently motionless grain matrix, are displayed in Figs. 2(b) and 2(d) (black arrows). The slow bubble motion observed between $t = 2.5$ h and $t = 11$ h is discussed in Sec. V. Note that these bubbles may also be eventually captured back inside the fluidized zone [Figs. 2(c) and 2(d)].

B. Bubble trajectories

Figure 3(a) displays different bubble trajectories. To get the contour of the fluidized region, we use the previous determination by Varas *et al.* [33] and Ramos *et al.* [27], based on a parabolic fit of its contour, $z = x^2/D$, where the coefficient D depends mainly on the injected flow rate Q, although its dependence on the grain size can be discussed [33]. Plotting z as a function of $x/\sqrt{D}$ makes it possible to superimpose on the same graph fluidized regions of different size, obtained when varying the flow rate Q [Fig. 3(a); gray zone]. Bubbles, initially created on the top part of the granular bed ($z > 15$ cm), follow a downward motion as they are entrained by the global granular convection in the central region [Fig. 3(a); white and gray squares]. To quantify the departure from a parabolic trajectory, we represent in the inset its normalized trajectory, ζ_z as a function of ζ_x^2, with

$$\zeta_x = \frac{(x - x_{\min})}{(x_{\max} - x_{\min})}, \tag{3}$$

$$\zeta_z = \frac{(z - z_{\min})}{(z_{\max} - z_{\min})}, \tag{4}$$

where $(x_{\max}, z_{\max})$ and $(x_{\min}, z_{\min})$ represent the first and last points of the bubble trajectory, from its creation until its capture by the central air channel [hatched zone; Fig. 3(a)], whose typical width is about 1 cm [see, for instance, Figs. 2(b) and 2(d)]. Bubbles initially trapped inside the fluidized zone follow an almost-vertical motion before collapsing onto a parabolic trajectory [red line; Fig. 3(a), upper-left inset]. Interestingly, the bubbles initially on the fluidized-zone border (or even slightly outside) follow an almost-perfect parabolic trajectory [red line; Figure 3(a), lower-right inset].

Figure 3(b) represents the velocity of three bubbles initially located in a close neighborhood [same symbols as the trajectories represented in Fig. 3(a)]. For bubbles located at

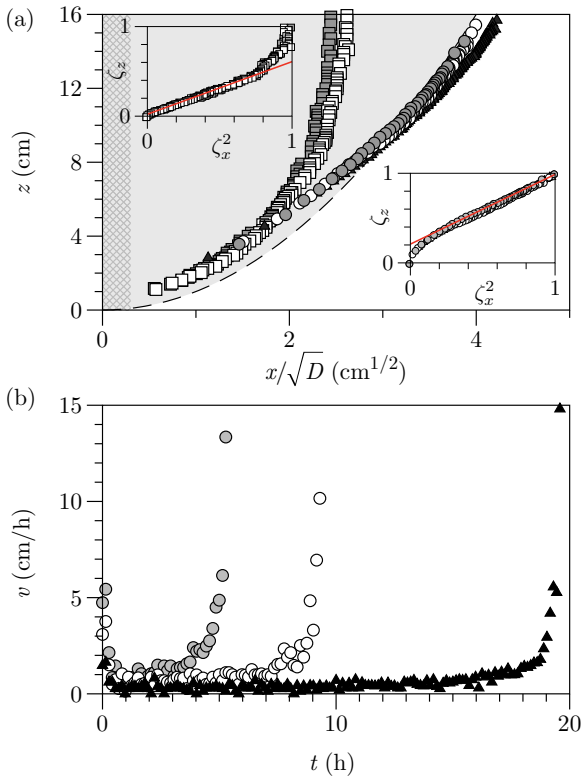

FIG. 3. Bubble dynamics [$d = 318 \pm 44$ μm, $Q = 0.66$ mL/s (white and gray squares) and $Q = 1.98$ mL/s (white and gray circles, black triangles]. (a) Examples of bubble trajectories. The altitude z is represented as a function of $x/\sqrt{D}$, so that parabolic fluidized regions of different size, for different Q, are superimposed. The hatched zone represents the central air rise. Inset: Normalized trajectory ζ_z vs ζ_x^2 (see text) for bubbles inside (top left) or close to the border of (bottom right) the fluidized zone. (b) Velocity of the bubbles located close to the fluidized-zone border (a). In spite of their close initial locations, the bubbles exhibit very different survival times. Note that the bubble initially outside the fluidized zone (black triangles) exhibits slow motion and is finally captured back by the central air channel.

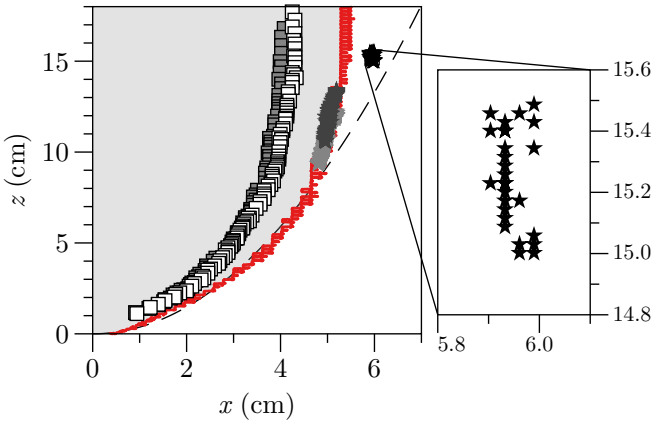

FIG. 4. Bubble trajectories and determination of the fluidized-zone boundary ($d = 318 \pm 44$ μm, $Q = 0.66$ mL/s). The dashed black line indicates the determination from a parabolic contour fit [27], while the red (light color) line represents the fluidized region boundary computed from the grain motion without any assumption (see Sec. IV B). Squares represent bubble trajectories inside the fluidized zone (light-gray region; same symbols as in Fig. 3), while stars represent bubble positions close to the real fluidized-zone boundary (light- and dark-gray stars) or between this boundary and the parabolic contour from a previous determination (black stars).

the border, a very small difference in their initial location has a drastic consequence on their survival time, which can vary from 5 to 20 h. The fact that a bubble initially trapped outside the fluidized zone can also move—although very slowly—is discussed in Sec. V B.

Previous work pointed out bubbles as tracers of the granular convection taking place in the fluidized zone [27,32]. As such, it would seem natural for their trajectory to follow a roughly parabolic shape—the shape of the fluidized region border, which constrains the granular flow. Why bubbles trapped inside the fluidized zone exhibit such a vertical motion at the beginning, in apparent contradiction with the global convective motion, is unraveled in Fig. 4. The contour of the fluidized region, previously determined from a parabolic contour fit, is represented as the dashed line, while the real fluidized zone, determined in Sec. IV B, is displayed in red (light) color. The departure from the parabolic contour is clearly shown not only close to the surface, but for almost the whole upper half of the granular bed. A few bubble positions are represented over the whole experimental time, typically $t \simeq 20$ h (Fig. 4). The light-gray, dark-gray, and black stars represent the group of bubbles indicated by the black arrow in Fig. 2. Interestingly, all bubbles follow a trajectory similar to the shape of the fluidized-zone border, although bubbles on or outside the latter exhibit very slow motion and sometimes do not move significantly over the experimental time (black stars; Fig. 4, inset).

In spite of the similarities of their trajectories, the bubbles exhibit strong differences in their dynamics and survival time. In the following, we therefore consider global quantities, to characterize the properties of the gas trapped in the fluidized bed and the three-phase contact area.

IV. GLOBAL PARAMETERS IN THE STATIONARY REGIME

A. Existence of a stationary state

In this section, we focus on global parameters characterizing the fluidized zone and their dependence on the experimental parameters: the fluidized-zone area S_{FZ} (Sec. IV B), the air volume $S_a e$ and volume fraction $\phi_a = S_a/S_{FZ}$ in the fluidized zone (Sec. IV C), and the three-phase contact area $\mathcal{C}$ (Sec. IV D). The bubbles outside the fluidized-zone area are not considered, as their number and size strongly depend on the initial air invasion dynamics, which is hardly reproducible.

Figure 5 displays an example of the evolution of ϕ_a as a function of time. The dashed red line shows the average computed over the last 15 h, $\phi_a = 2.03 \pm 0.40\%$. Although the signal strongly fluctuates in time, after a transient regime (Fig. 5, inset), the system reaches a stationary state during which global parameters can be determined. In the following sections, we investigate these global parameters and their dependence on the flow rate and grain size.

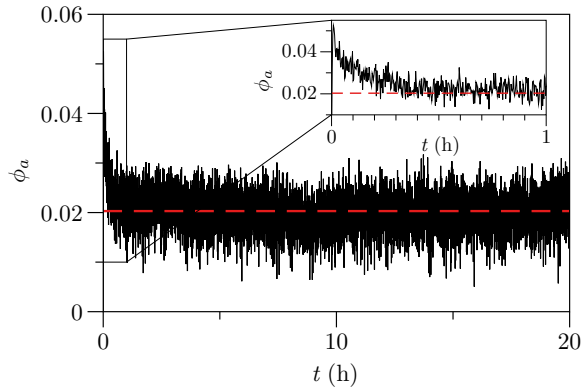

FIG. 5. Temporal evolution of the air volume fraction in the fluidized zone ($d = 318 \pm 44$ μm, $Q = 1.98$ mL/s). The dashed red line represents the average of the signal computed over the last 15 h, $\phi_a \simeq 2\%$. The standard deviation over the same time window is 0.4%. Inset: Zoom-in on the transient regime.

B. Area of the fluidized zone

Previous works have pointed out the parabolic shape of the central fluidized zone, $z = x^2/D$, and determined the variations of D as a function of the typical grain size and the air injection flow rate (see, for example, [33]). However, although the parabolic shape fits well the data over a large region above the injection point, discrepancies are observed close to the grain's free surface (see, for instance, Fig. 4 of Varas *et al.* [33] and Sec. III B here). Because this study aims at determining the global characteristics of the fluidized zone, without any assumption about its shape, we extend the method introduced by Ramos *et al.* [27] to compute its area.

The fluidized zone is characterized by a slow grain motion, and its dynamics can be captured by summing consecutive image differences:

$$\rho_n(x,z) = \sum_{k=1}^{n-1} |\mathrm{I}_{k+1} - \mathrm{I}_k|. \tag{5}$$

The parameter ρ_n was introduced as the *flow density*, as it provides a cartography of the global motion over the whole experimental cell [27,33]. For all data sets, the flow density was computed over the last 4000 images of the experiments (cumulating $\sim$11 h of data), to avoid the transient, ensure the fluidized region has reached its stationary shape [27], and obtain a good contrast in the flow density map. A simple binarization makes it possible then to compute the fluidized-zone area. The threshold used for binarizing has to be adjusted to each data set, as the value of $\rho_n(x,z)$ strongly depends on Q, a low flow rate producing much less motion than a high flow rate between two consecutive images. A postprocessing check is performed by superimposing the fluidized-zone boundaries of the successive images and accelerating the video about $100\times$ to verify that the motion is located between the computed boundaries. Examples of fluidized-zone contour determination are displayed in Figs. 2(b) and 2(d) (gray lines) and Fig. 4 (red line).

In addition to avoiding any assumption about the fluidized-zone boundaries shape, this method also accounts for the deformation of the granular bed free surface. Indeed, due to the presence of bubbles inside the central zone, this surface is slightly bulged and fluctuates in time due to the successive bubble passages. The error bars on the fluidized-zone area determination are taken as the standard deviation of these fluctuations.

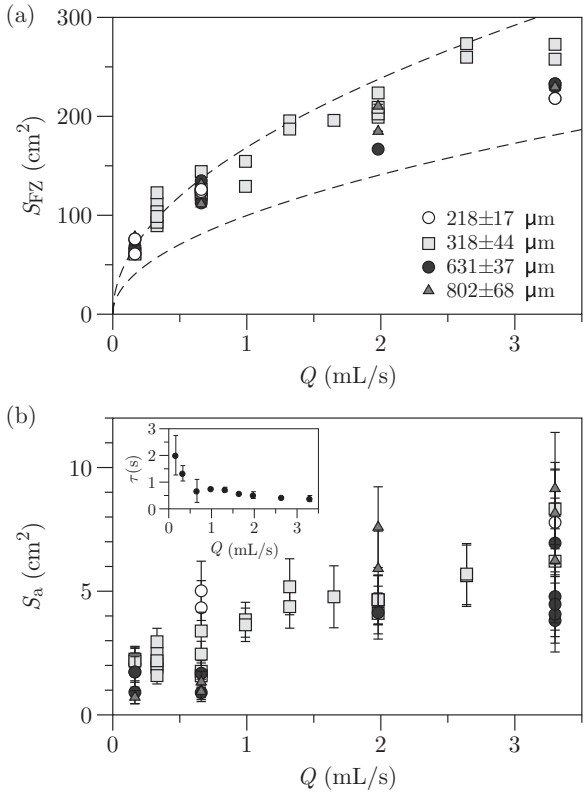

FIG. 6. (a) Area of the central fluidized zone as a function of the flow rate Q, for different grain sizes (error bars are the size of the symbols or smaller). Dashed black lines indicate the predicted fluidized-zone area S^*_{FZ} from a previous determination of its parabolic contour (see text) [bottom line, $\alpha = 0.7$; top line, $\alpha = 2$]. (b) Apparent area of the air inside the fluidized zone as a function of the flow rate Q, for different grain sizes. Inset: Mean residence time $\tau = \langle S_a \rangle e/Q$ of the gas inside the granular bed.

Figure 6(a) displays the fluidized-zone area, S_{FZ}, as a function of the air injection flow rate Q, for the four grain batches. S_{FZ} increases with the flow rate but does not depend significantly on the grain size d. Qualitatively, the more strongly the air is injected through the granular bed, the larger the global grain motion in the central zone will be. This result is in agreement with a previous study which determined the size of the fluidized zone based on a parabolic contour determination, $z = x^2/D$, where D was found to increase with Q [33]. Note that the fluctuations of the fluidized-zone area are very small, at most a few percent of S_{FZ} [the error bars in Fig. 6(a) are the size of the symbols or smaller].

Considering that the empirical variation of D as a function of Q can be approximated, at first order, by a linear function (see Fig. 5(a) in Ref. [33]), $D = \alpha Q$, a theoretical estimation of the fluidized-zone area can be made,

$$S^*_{FZ} = 2\int_0^{h_g} \sqrt{Dz}\, \mathrm{d}z = \frac{4}{3}\sqrt{\alpha}\, h_g^{3/2}\sqrt{Q}, \tag{6}$$

where $h_g = 20$ cm is the height of the granular bed. The variation of S^*_{FZ} as a function of the flow rate is reported in Fig. 6(a) for the two extreme values of the empirical parameter α ($\alpha = 0.7$ cm^{-2} s, lower dashed line; and $\alpha = 2$ cm^{-2} s, upper dashed line). The results are in good agreement. Although a departure from the parabolic contour is clearly observed, in particular, close to the surface (Sec. III B), the area computed with the above method lies in the range predicted by the parabolic shape assumption and previous empirical determination of the coefficient D.

C. Gas volume fraction in the fluidized zone

The average air volume inside the fluidized zone, $S_a e$, is computed by estimating the apparent air surface area, S_a, multiplied by the gap e. The validity of this approximation is checked in the Discussion (Sec. V A). A simple image analysis (binarization) combined with the previous determination of the central fluidized zone makes it possible, first, to isolate the bubbles inside the fluidized region and, then, to compute their apparent surface and volume. Figure 6(b) displays the evolution of the average gas apparent surface area, S_a, as a function of the flow rate Q. The error bars represent the standard deviation, directly linked to the amplitude of the fluctuations (see Sec. IV A and Fig. 5). Similarly to S_{FZ}, S_a increases when Q increases and does not depend significantly on the grain size. Note that the fluctuations slightly increase with Q and are of the same order of magnitude as the fluctuations in amplitude for S_{FZ} (~ 1 cm^2). Indeed, by simple mass conservation, the variations of gas content in the fluidized zone have a direct signature on the modulations of the granular bed free surface.

A standard way to compute global quantities in three-phase flows is to consider the residence time of a phase (e.g., the gas phase) inside the system [14]. It is defined as the time a given gas bubble, for instance, will remain in the immersed granular bed, from the moment it is injected until it is driven out of the grains. The mean residence time of the gas inside the granular bed can be computed as $\tau = \langle S_a \rangle e/Q$ [Fig. 6(b), inset], where $\langle S_a \rangle$ indicates the average over the different experiments at a fixed flow rate (different runs or grain batches). τ strongly decreases with Q up to $Q \simeq 1$ mL/s, after which it remains roughly constant and of the order of 0.5 s. This value is difficult to interpret, as it accounts for two very different time scales: (i) a fast-rising air channel or bubbles at the vertical of the injection nozzle (central part of the cell) and (ii) slow granular convection entraining the bubbles for several hours in the fluidized zone (see Sec. III). The small value of τ, of the order of a second, hints at considering the central air channel as the main process driving air through the system.

The air volume fraction in the fluidized region is then computed as $\phi_a = S_a/S_{FZ}$ (Fig. 7). Interestingly, in spite of some dispersion of the data, ϕ remains roughly constant when Q varies. In other words, increasing the flow rate does increase the average volume of gas trapped in the "active" central zone, but because the latter widens with large Q, the gas volume fraction trapped inside remains on average constant, $\phi_a = 2.3 \pm 0.9\%$.

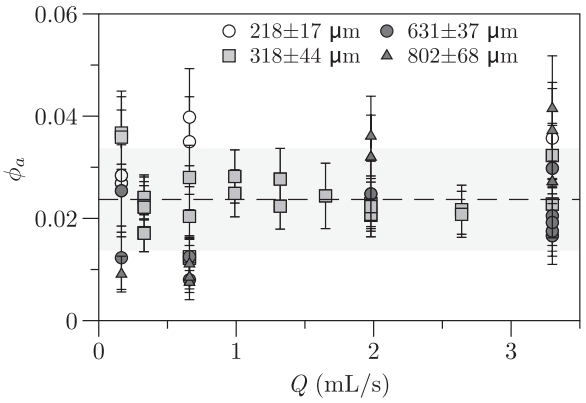

FIG. 7. Gas volume fraction in the fluidized zone as a function of the flow rate Q, for different grain batches. Error bars represent the fluctuations in the stationary state (see text). The dashed line and the light-gray zone represent the average of all the data and their standard deviation, $\phi_a = 2.3 \pm 0.9\%$.

D. Contact area

In terms of potential applications—for instance, in catalytic reactions and chemical engineering processes—it is interesting to investigate the contact area among the three phases, namely, gas (air), liquid (water), and solid (grains). From the images, we compute the contact area, $\mathcal{P}_a e$, where $\mathcal{P}_a$ is the average perimeter of the bubbles in the stationary regime. To get a quantification of the transfer function of the system (ratio of the output to the input of the experiment), this quantity is normalized by S_a, which is a good approximation of the system input in terms of contact area.

Figure 8 represents the normalized contact area, $\mathcal{C} = \mathcal{P}_a e/S_a$, as a function of the flow rate Q. Although the data are scattered for low flow rates ($Q < 1$ mL/s), $\mathcal{C}$ does not exhibit strong variations. It decreases slightly with the flow rate and reaches a plateau at $\mathcal{C} \simeq 2$ for $Q > 1$ mL/s. This behavior is clearly seen when averaging $\mathcal{C}$ over the different experiments (different runs or different grain sizes) for a given flow rate Q (Fig. 8, inset).

Therefore, within the experimental error bars, the normalized contact area does not depend significantly on the gas

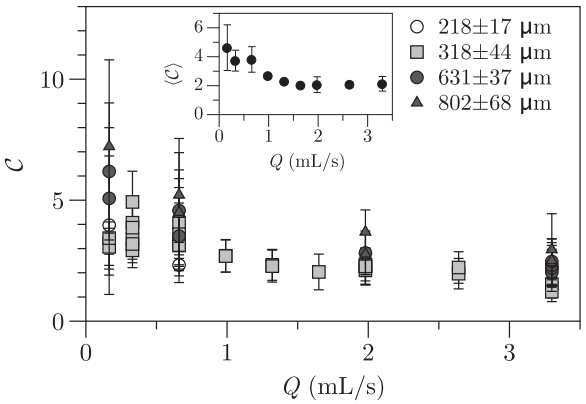

FIG. 8. Normalized contact area $\mathcal{C} = \mathcal{P}_a e/S_a$ as a function of the flow rate Q. Inset: Average normalized contact area, $\langle \mathcal{C} \rangle$, as a function of the flow rate Q.

injection flow rate. This result can be explained qualitatively, based on the observation of air invasion regimes in the system, in the stationary state. A possible interpretation is in terms of typical bubble size (radius), r_b, which can be defined as $S_a = N_b \pi r_b^2$, where N_b is the typical number of bubbles in the fluidized zone. By writing $\mathcal{P}_a = 2N_b \pi r_b$, one gets $r_b = 2e/\mathcal{C}$. For $Q > 1$ mL/s, $\mathcal{C}$ is roughly constant ($\mathcal{C} \simeq 2$), meaning that the average bubble size in the fluidized zone does not vary much ($r_b \simeq 2$ mm)—only their number increases. In that case, the air crosses the system mainly as spherical or elongated bubbles. The scattering and global trend of $\mathcal{C}$ for $Q < 1$ mL/s indicates a decrease in r_b with decreasing Q. Indeed, at low flow rates, the air tends to rise through the fluidized zone by percolation-like events, with a shape becoming more and more fractal when Q decreases, leading to a stronger increase in $\mathcal{P}_a/S_a$ and, thus, in $\mathcal{C}$.

V. DISCUSSION

A. Bubble volume estimatiom

In Sec. IV C, the air volume trapped in the fluidized zone was computed as $S_a e$, where S_a is the apparent surface of the bubbles, as measured from image analysis, and e the cell gap. This approximation holds true as long as two conditions are checked. First, the bubble radius r_b must be such that $r_b > e$, to ensure that the main part of the bubble volume is not in its lateral menisci. The estimation in Sec. IV D provides a typical bubble radius $r_b \simeq 0.8$–2 mm ($\mathcal{C} \simeq 2$–5), of the order of the cell gap. However, one must keep in mind that the estimation of an average bubble radius r_b takes into account the multiplicity of bubble contours, including very fractal bubbles or air fingers. It therefore biases the mean radius estimation toward small values, which are not representative of the real bubble size in the system [see, for example, Figs. 2(b) and 2(d), where for most bubbles, $r_b \simeq 5$–10 mm, much larger than the cell gap].

The second condition to be checked is that the lubrication layer, i.e., the thin liquid film between the bubble and the glass plate, has a volume negligible with respect to the bubble volume. An estimation of the thickness of the lubrication film thickness, h, is provided in Ref. [38]:

$$\frac{h}{e} \sim \frac{\mathrm{Ca}^{2/3}}{1 + \mathrm{Ca}^{2/3}}, \tag{7}$$

where $\mathrm{Ca} = \eta U/\gamma$ is the capillary number, η the fluid viscosity, U the typical bubble velocity, and $\gamma = 72$ mN/m the air-water surface tension. The bubble velocity varies from $U \sim 1$ cm/h in the fluidized zone [Fig. 3(b)] up to $U \sim 1$ cm/s in the central air channel. Estimating the effective viscosity is challenging, as it strongly depends on the grain packing fraction, which may vary in our system. To get a rough estimation, we use the semiempirical model of Zarraga *et al.* [39], which predicts the viscosity of dense suspensions up to a grain packing fraction $\phi_g \simeq 60\%$: $\eta = \eta_w e^{-2.34\phi_g}/(1 - \phi_g/\phi_g^*)^3$, where $\eta_w = 10^{-3}$ Pa.s is the water viscosity and $\phi_g^* = 62\%$ is the maximum packing fraction (poured random packing). By considering $\phi_g \simeq 56\%$ in the fluidized zone (very loose random packing), we get an effective viscosity of $\eta \simeq 0.3$ Pa.s. The capillary number therefore lies in the range $\mathrm{Ca} \simeq 10^{-5}$ to 4×10^{-2}, leading to $h \ll e$ [Eq. (7)].

The approximation of the air volume in the fluidized zone as $S_a e$ is therefore justified, and the error introduced by smaller bubbles and/or higher velocities (for higher flow rates) is smaller than a few percent.

B. Bubbles outside the fluidized zone: Trapped or not trapped?

It is commonly accepted that granular systems can exhibit solid, liquid, or even gas behavior [40,41]. In this study, as in previous works on gas or liquid injection in a dry or immersed granular layer [18,21,31,42,43], we separated the granular bed into a fluid-like region, at the center, surrounded by a solid-like region. We mentioned, in particular, that bubbles initially formed outside the fluidized zone remained trapped permanently in the system (Sec. III). However, Figs. 2(c), 2(d), and 3(a) display the trajectory of a bubble, although the latter is initially slightly outside the fluidized-zone boundaries. This bubble takes a long time to move downwards and is finally captured by the central air channel at $t \sim 20$ h [Fig. 2(c)]. The bubble location outside of the so-called fluidized zone is not due to an error in the determination of its contour, as two different methods (parabolic fit or motion localization), although giving slightly different boundaries, both locate the bubble in the solid-like region.

Another example is given by the group of bubbles pointed out by the black arrow in Fig. 2(b). These bubbles are initially formed either at the boundary of or outside the solid-like region. Although their horizontal position does not vary much in time, and they appear to be trapped [Fig. 2(a), upper panel], the spatiotemporal diagram in z shows a very slow drift downward [Fig. 2(a), lower panel], which can be appreciated by comparing the pictures taken at $t \sim 2.5$ h and $t \sim 11$ h [Fig. 2(b); black arrows].

The so-called solid-like region therefore experiences very slow motion, which can be seen only by running the experiment over a long time scale. This motion can be interpreted as creep flow, analogous to that reported in avalanches or sediment transport where, below the flowing layer, an exponential velocity decrease has been evidenced [44–47]. A thorough study of the creep motion in our experiment would require running the experiment over a much longer time, which is beyond the scope of this work.

C. Generalization to 3D systems

Previous works have addressed the comparison of a fluidized-zone formation by air injection in an immersed granular layer in quasi-2D and 3D systems [31]. They pointed out, first, the similarity of the parabolic shape for the fluidized-zone boundary and, second, the fact that its extent is smaller in three dimensions than in two, mainly due to geometrical effects. Although this result was expected, predicting the dynamics of 3D systems from 2D or quasi-2D experiments is far from trivial. In particular, adding one degree of freedom could lead to a weaker air channel stabilization, which could possibly result in an increase in bubble generation and a higher air volume fraction in the fluidized zone. A full study of a

3D system is required to extend the results of this work to unconfined media.

VI. CONCLUSION

This study has focused on the local and global dynamics of air injected at a constant flow rate at the bottom of an immersed granular material confined in a quasibidimensional cell. After a transient, a central fluidized zone is formed, characterized by a central air rise and a global grain motion in the form of two convection rolls. We investigated the dynamics of the bubbles trapped in the granular bed. In the stationary regime, most of the gas in the system is in the central air rise, consisting of a localized channel of about 1 cm width. Other bubbles are either formed initially, during the transient, or further generated by lateral explorations of the central air channel. Contrary to intuition, these bubbles do not rise but are entrained by the downward granular motion, until they are captured back by the central air rise. They follow trajectories characterized first by a roughly vertical motion and then by a parabolic function. A more accurate determination of the fluidized region showed that these trajectories roughly follow the shape of the fluidized-zone boundary.

Interestingly, the solid-like region outside the fluidized zone exhibits a slow motion, over a much longer time scale (typically, a few tens of hours). This creep flow also seems to follow a trajectory similar to the fluidized-zone boundary, until the bubble is eventually captured back by the central channel, close to the cell bottom. Further investigation of this creep motion would require much longer experiments and a very slow-motion tracking technique, which should be the topic of future work.

The analysis of global parameters in the stationary regime pointed out an increase in both the size of the fluidized zone and the quantity of air trapped in the system when the flow rate is increased. Interestingly, the gas volume fraction in the fluidized zone remains roughly constant, at about 2%–3%. This order of magnitude corresponds roughly to the size of the channel, which is where most of the air is concentrated. Other bubbles around are only created by rare events and are small enough to remain trapped in the system for some time.

Finally, the normalized contact area among the three phases does not depend significantly on the flow rate. This result has strong implications, for instance, in chemical engineering, where a large contact area is fundamental to increasing the efficiency of a catalytic reaction. This work points out that, contrary to intuition, increasing the injection flow rate does not increase the efficiency of the reaction and that an optimum has to be found by varying other parameters, for instance, by a joint gas-and-liquid flow, or by considering several gas injection points.

ACKNOWLEDGMENTS

G. Varas acknowledges financial support from FONDECYT Project No. 11121300. This work was supported by Programa de Cooperación Científica ECOS/CONICYT C14E07.

[1] R. Richards, Jr., D. G. Elms, and M. Budhu, Dynamic fluidization of soils, J. Geotech. Eng. **116**(5), 740 (1990).

[2] M. Hovland, J. V. Gardner, and A. G. Judd, The significance of pockmarks to understanding fluid flow processes and geohazards, Geofluids **2**, 127 (2002).

[3] A. Gay, M. Lopez, P. Cochonat, M. Sérane, D. Levaché, and G. Sermondadaz, Isolated seafloor pockmarks linked to BSRs, fluid chimneys, polygonal faults and stacked Oligocene Miocene turbiditic palaeochannels in the Lower Congo Basin, Mar. Geol. **226**, 25 (2006).

[4] S. Planke, H. Svensen, M. Hovland, D. A. Banks, and B. Jamtveit, Mud and fluid migration in active mud volcanoes in Azerbaijan, Geo-Mar. Lett. **23**, 258 (2003).

[5] V. Mastalerz, G. J. de Lange, A. Dählmann, and T. Feseker, Active venting at the Isis mud volcano, offshore Egypt: Origin and migration of hydrocarbons, Chem. Geol. **246**, 87 (2007).

[6] A. Mazzini, H. Svensen, G. G. Akhmanov, G. Aloisi, S. Planke, A. Malthe-Sørenssen, and B. Istadi, Triggering and dynamic evolution of the LUSI mud volcano, Indonesia, Earth Planet. Sci. Lett. **261**, 375 (2007).

[7] A. L. Walters, J. Phillips, R. J. Brown, M. Field, T. Gernon, G. Stripp, and R. S. J. Sparks, The role of fluidisation in the formation of volcaniclastic kimberlite: Grain size observations and experimental investigation, J. Volcanol. Geotherm. Res. **155**, 119 (2006).

[8] T. M. Gernon, M. A. Gilbertson, R. S. J. Sparks, and M. Field, Gas-fluidisation in an experimental tapered bed: Insights into processes in diverging volcanic conduits, J. Volcanol. Geotherm. Res. **174**, 49 (2008).

[9] T. M. Gernon, R. S. J. Sparks, and M. Field, Degassing structures in volcaniclastic kimberlite: Examples from southern African kimberlite pipes, J. Volcanol. Geotherm. Res. **174**, 186 (2008).

[10] J. S. Selker, M. Niemet, N. G. McDuffie, S. M. Gorelick, and J.-Y. Parlange, The local geometry of gas injection into saturated homogeneous porous media, Transp. Porous Med. **68**, 107 (2007).

[11] R. Semer, J. A. Adams, and K. R. Reddy, An experimental investigation of air flow patterns in saturated soils during air sparging, Geotech. Geol. Eng. **16**, 59 (1998).

[12] K. R. Reddy, R. Semer, and J. A. Adams, Air flow optimization and surfactant enhancement to remediate toluene-contaminated saturated soils using air sparging, Environ. Manage. Health **10**, 52 (1999).

[13] G. Biardi and G. Baldi, Three-phase catalytic reactors, Catal. Today **52**, 223 (1999).

[14] K. Pangarkar, T. J. Schildhauer, J. Ruud van Ommen, J. Nijenhuis, F. Kapteijn, and J. A. Moulijn, Structured packings for multiphase catalytic reactors, Ind. Eng. Chem. Res. **47**, 3720 (2008).

[15] A. R. Dexter, Advances in characterization of soil structure, Soil Till. Res. **11**, 199 (1988).

[16] J. M. Valverde and A. Castellanos, Types of gas fluidization of cohesive granular materials, Phys. Rev. E **75**, 031306 (2007).

[17] A. Nermoen, C. Raufaste, S. D. de Villiers, E. Jettestuen, P. Meakin, and D. K. Dysthe, Morphological transitions in partially gas-fluidized granular mixtures, Phys. Rev. E **81**, 061305 (2010).

[18] A. Nermoen, O. Galland, E. Jettestuen, K. Fristad, Y. Podladchikov, H. Svensen, and A. Malthe-Sørenssen, Experimental and analytic modeling of piercement structures, J. Geophys. Res. **115**, B10202 (2010).

[19] P. Rigord, A. Guarino, V. Vidal, and J.-C. Géminard, Localized instability of a granular layer submitted to an ascending liquid flow, Gran. Matter **7**, 191 (2005).

[20] T. Wilhelm and K. Wilmański, On the onset of flow instabilities in granular media due to porosity inhomogeneities, Int. J. Multiphase Flow **28**, 1929 (2002).

[21] T. Mörz, E. A. Karlik, S. Kreiter, and A. Kopf, An experimental setup for fluid venting in unconsolidated sediments: New insights to fluid mechanics and structures, Sediment. Geol. **196**, 251 (2007).

[22] F. Zoueshtiagh and A. Merlen, Effect of a vertically flowing jet underneath a granular bed, Phys. Rev. E **75**, 056313 (2007).

[23] Ø. Johnsen, C. Chevalier, A. Lindner, R. Toussaint, E. Clément, K. J. Måløy, E. G. Flekkøy, and J. Schmittbuhl, Decompaction and fluidization of a saturated and confined granular medium by injection of a viscous liquid or gas, Phys. Rev. E **78**, 051302 (2008).

[24] C. Chevalier, A. Lindner, M. Leroux, and E. Clément, Morphodynamics during air injection into a confined granular suspension, J. Non-Newtonian Fluid Mech. **158**, 63 (2009).

[25] B. Sandnes, E. G. Flekkoøy, H. A. Knudsen, K. J. Måløy, and H. See, Patterns and flow in frictional fluid dynamics, Nature Comm. **2**, 288 (2011).

[26] P. Philippe and M. Badiane, Localized fluidization in a granular medium, Phys. Rev. E **87**, 042206 (2013).

[27] G. Ramos, G. Varas, J.-C. Géminard, and V. Vidal, Gas-induced fluidization of mobile liquid-saturated grains, Phys. Rev. E **92**, 062210 (2015).

[28] W. Ji, A. Dahmani, D. P. Ahlfeld, J. D. Lin, and E. Hill, Laboratory study of air sparging: air flow visualization, Ground Water Monit. Rem. **13**, 115 (1993).

[29] K. R. Reddy, S. Kosgi, and J. Zhou, A review of in-situ air sparging for the remediation of VOC-contaminated saturated soils and groundwater, Hazard. Waste Hazard. Mater. **12**, 97 (1995).

[30] X.-Z. Kong, W. Kinzelbach, and F. Stauffer, Migration of air channels: An instability of air flow in mobile saturated porous media, Chem. Eng. Sci. **64**, 1528 (2009).

[31] G. Varas, V. Vidal, and J.-C. Géminard, Venting dynamics of an immersed granular layer, Phys. Rev. E **83**, 011302 (2011).

[32] G. Varas, J.-C. Géminard, and V. Vidal, Air invasion in a granular layer immersed in a fluid: Morphology and dynamics, Gran. Matter **15**, 801 (2013).

[33] G. Varas, G. Ramos, J.-C. Géminard, and V. Vidal, Flow and fracture in water-saturated, unconstrained granular beds, Front. Phys. **3**, 44 (2015).

[34] S. E. Roosevelt and M. Y. Corapcioglu, Air bubble migration in a granular porous medium: Experimental studies, Water Resour. Res. **34**, 1131 (1998).

[35] M. Y. Corapcioglu, A. Cihan, and M. Drazenovic, Rise velocity of an air bubble in porous media: Theoretical studies, Water Resour. Res. **40**, W04214 (2004).

[36] M. Stohr and A. Khalili, Dynamic regimes of buoyancy-affected two-phase flow in unconsolidated porous media, Phys. Rev. E **73**, 036301 (2006).

[37] G. Varas, V. Vidal, and J.-C. Géminard, Dynamics of crater formations in immersed granular material, Phys. Rev. E **79**, 021301 (2009).

[38] M. Roudet, *Hydrodynamique et transfert de masse autour d'une bulle confinée entre deux plaques*, Ph.D. thesis, Institut National Polytechnique de Toulouse (2008).

[39] I. E. Zarraga, D. A. Hill, and D. T. Leighton, The characterization of the total stress of concentrated suspensions of noncolloidal spheres in Newtonian fluids, J. Rheol. **44**, 185 (2000).

[40] Y. Amarouchène, J. F. Boudet, and H. Kellay, Dynamic Sand Dunes, Phys. Rev. Lett. **86**, 4286 (2001).

[41] Y. Forterre and O. Pouliquen, Flow of dense granular media, Annu. Rev. Fluid Mech. **40**, 1 (2008).

[42] W. Zhong and M. Zhang, Jet penetration depth in a two-dimensional spout-fluid bed, Chem. Eng. Sci. **60**, 315 (2005).

[43] X.-Z. Kong, W. Kinzelbach, and F. Stauffer, Morphodynamics during air injection into water-saturated movable spherical granulates, Chem. Eng. Sci. **65**, 4652 (2010).

[44] T. S. Komatsu, S. Inagaki, N. Nakagawa, and S. Nasuno, Creep Motion in a Granular Pile Exhibiting Steady Surface Flow, Phys. Rev. Lett. **86**, 1757 (2001).

[45] G. D. R. Midi, On dense granular flows, Eur. Phys. J. E **14**, 341 (2004).

[46] S. Courrech du Pont, R. Fischer, P. Gondret, B. Perrin, and M. Rabaud, Instantaneous Velocity Profiles during Granular Avalanches, Phys. Rev. Lett. **94**, 048003 (2005).

[47] M. Houssais, C. P. Ortiz, D. J. Durian, and D. J. Jerolmack, Onset of sediment transport is a continuous transition driven by fluid shear and granular creep, Nature Comm. **6**, 6527 (2015).